JOURNAL OF SPACECRAFT AND ROCKETS
Vol. 35, No. 1, January–February 1998

Influence of Crossflow and Turbulence on Vortex Flow Around a Supersonic Missile

F. Grasso*
University of Rome "La Sapienza," Rome 00184, Italy
and
G. Iaccarino†
Centro Italiano Ricerche Aerospaziali, Capua (CE) 81043, Italy

A three-dimensional Reynolds averaged Navier–Stokes solver is applied to analyze the aerodynamic behavior of supersonic missile configurations in the presence of crossflow. The model employs a low Reynolds k–ϵ model and relies on a finite volume multiblock strategy that exploits local grid refinement. A large set of experimental data is used to validate the simulations and to verify the grid sensitivity of the solutions. An analysis of the skin-friction pattern and of the crossflow vortex structures at different angles of attack shows that the influence of turbulence is strong only for low incidence. At higher angles of attack, the flow is dominated by streamwise vorticity production.

Nomenclature

$C_\mu, C_{\epsilon_1}, C_{\epsilon_2}$	= constants of the turbulence model
D	= body dimension
E	= total energy
e	= internal energy
k	= turbulence kinetic energy
M	= Mach number
N	= number of grid points; nodes
P	= production
Pr	= Prandtl number
p	= pressure
q_j	= total heat flux component
Re	= Reynolds number
S	= saddle points
S_{ij}	= component of symmetric part of strain tensor
u_i	= Cartesian velocity component
x, y, z	= Cartesian coordinates
α	= angle of attack
γ	= specific heat ratio
δ_{ij}	= Kronecker delta
ϵ	= dissipation of turbulence kinetic energy
θ	= azimuthal direction
μ	= viscosity
ρ	= density
σ_{ij}	= component of total stress tensor
Φ	= dissipation
Ω	= streamwise vorticity

Subscripts

i	= direction
t	= turbulent
x, r, θ	= axial, radial, and azimuthal directions
∞	= freestream

Superscripts

$'$	= fluctuation; half-critical point
$''$	= Favre fluctuation
$\bar{(\ )}$	= time average
$\tilde{(\ )}$	= Favre average

Received March 4, 1997; revision received June 18, 1997; accepted for publication June 18, 1997.

*Associate Professor, Department of Mechanics and Aerodynamics, via Eudossiana 18. Associate Fellow AIAA.

†Research Scientist, Department of Aerodynamics and Propulsion, via Maiorise. Member AIAA.

Introduction

THE development of high-velocity vehicles, i.e., supersonic transport airplanes, launchers, re-entry vehicles, etc., has refocused attention on the problem of accurately predicting 1) shock-wave/boundary-layer interaction phenomena, 2) the influence of transition, 3) turbulence, and 4) vortical flows, etc. These phenomena constitute a challenge for both theoreticians and experimentalists. Indeed, on one hand, there are many open questions regarding appropriate physical models, especially for turbulence. (In addition, even for those phenomena for which models exist, difficulties remain regarding the simulation aspect.) On the other hand, the experimental investigations rely on wind-tunnel tests that in most circumstances yield a limited amount of detailed information.

In the present work we focus our attention on the analysis of the flow around missile configurations in the supersonic regime. Traditionally, the design of the missile forebody has relied heavily on experimental testing and semiempirical procedures.[1] The use of such approaches has generally been favored because the influence of design parameters can be quickly predicted and optimized. Navier–Stokes solvers, however, have the potential of being able to model the flow features at a more fundamental level. These techniques can provide a high level of detail that may help the aerodynamicist not only to predict the vehicle performance but also to shed light on the reasons why the physics produces a certain type of aerodynamic behavior, useful, in particular, for missile flows that are dominated by the presence of strong vortices in the leeside region.

Several papers on the subject have appeared.[2–8] In the late 1970s, an experimental database for computer program assessment was published by the Working Group WG-14 of AGARD,[2] which included surface pressure measurements over an ogive-cylinder geometry at various angle of attack and Mach numbers.

More recently, Pagan et al.[3] investigated the flow around an ogive cylinder at freestream supersonic Mach number, focusing on the influence of incidence and turbulence on the flowfield. In particular, they investigated the effects of both laminar and forced transition conditions, the latter obtained by means of a strip located close to the body apex. The experiments provide a large set of pressure measurements on the surface, obtained by means of pressure taps, and surface flow visualization, obtained by oil flow techniques, that allows an interpretation of the topology of the complex flow structure in terms of skin friction pattern and constitutes a basis for validating numerical simulations. Pagan et al.[3] show that the influence of turbulence is strongest at low incidence. In particular, at 5-deg incidence, the laminar flow shows a primary and a secondary

separation, whereas it is fully attached under turbulent conditions; at high angles of attack (>10 deg) the surface and crossflow measurements (pressure, Mach number, separation and reattachment, etc.) are very similar in both cases.

Some applications of Navier–Stokes solvers to this type of flow have been published: Degani and Shiff [4] have assessed the validity of a parabolized Navier–Stokes (PNS) solver that uses a modified Baldwin–Lomax (two-layer) turbulence model to compute turbulent supersonic flows around sharp-nose slender bodies at incidence. In the presence of crossflow separation, the standard Baldwin–Lomax model fails to properly identify the characteristic length scale of the outer layer because of its inability to discriminate between the characteristic length scales of the vortex shear layer and the boundary layer. Degani and Shiff [4] introduced a cutoff length to properly evaluate the viscous layer length, thus eliminating such ambiguity. By an extensive series of computations, they have shown an increase in accuracy in the crossflow separation region. In addition, they have also concluded that, to obtain accurate numerical simulations of vortical flows around slender bodies at incidence, both an adequate radial and circumferential resolution of the leeward vortices and an adequate resolution of the attached viscous layer are required. Moschetta et al.[5] presented an extensive study of the flow around an ogive cylinder at incidence assuming laminar conditions. They used a PNS flow solver and performed a grid sensitivity analysis of the crossflow topology of vortical structures. In particular, Ref. 5 showed that the latter are mostly influenced by the circumferential grid resolution and concluded that PNS solvers are adequate for predicting supersonic vortical flows around slender bodies, provided the grid is sufficiently refined.

Deniau et al.[6] studied the turbulent supersonic flow around axisymmetric bodies at moderate incidence by means of a PNS solver and presented an analysis of the influence of turbulence modeling (ranging from algebraic to two-equation models) and grid properties. In the presence of crossflow separation, they conclude that an improvement in the prediction of stagnation pressure level in the vortex core can be obtained by means of low Reynolds k–ϵ models (in comparison to zero-equation and two-layer k–ϵ models).

Birch et al.[7] analyzed the supersonic flow around a slender body at high incidence by solving either the Reynolds averaged Navier–Stokes (RANS) or PNS equations, together with a modified Baldwin–Lomax model as proposed by Degani and Shiff.[4] In particular, Birch et al.[7] studied the influence of grid resolution and parabolizing assumptions and showed that RANS and PNS results yield some small differences in the proximity of crossflow separation and in the leeside region. To isolate the influence of the grid from the turbulence, they performed simulations at a low Reynolds number (so as to assume laminar conditions), concluding that the quality of the results depends mainly on the radial and circumferential grid point distributions. For laminar conditions and independently of the grid, they observed a crossflow shock stronger than the experimental one.[7]

Numerical simulations may suffer from the lack of understanding of the controlling phenomena and/or inappropriate physical models, as well as limited experimental information. The cited numerical works are based mainly on the use of PNS flow solvers (a procedure generally followed for the simulation of missile aerodynamics). Weinacht and Sahu[8] recently reviewed the application of Navier–Stokes solvers to predict missile aerodynamics and pointed out that the parabolizing approximation is valid provided that 1) the upstream propagation through the subsonic portion of the boundary layer should not be significant, which requires that the freestream Mach number should be greater than 1.5–1.7; 2) the absence of streamwise separation, i.e., the missile geometry, should not present body discontinuities; and 3) the design of the nosecap should be such that the influence on the downstream flowfield is negligible, and, likewise, the details of the flow in the proximity of the nose region should not be important. We recall that, at high incidence and even for (geometrically simple) slender bodies, in the leeside region PNS results may show some differences with respect to the full Navier–Stokes results. We also recall that numerical simulations are strongly affected by the numerical methodology, i.e., accuracy, efficiency, physical and geometrical modeling, etc. The use of computational fluid dynamics then poses the question of how one can be sure of the accuracy of the computed solution, i.e., how reliable a solution is for the understanding of physical phenomena or for the estimation of critical issues. The reliability of a computed solution can be established only by validation.

In this paper we present an extensive analysis of the flow around an ogive cylinder by means of the full three-dimensional Reynolds averaged Navier–Stokes equations. The model developed is based on the low Reynolds k–ϵ equations and relies on a finite volume multiblock strategy that exploits local grid refinement. The computational method uses a physical operator adaptation strategy that allows solutions of the RANS equations only in the zones where diffusion effects are important. We carry out an analysis of the influence of the grid with the aim to give guidelines on the requirements of a computational mesh when both accuracy and efficiency constraints have to be met. An extensive comparison with experiments available in the literature is presented, together with an analysis of the influence of turbulence on surface pressure and crossflow separation.

Governing Equations

The governing equations are the full three-dimensional Navier–Stokes equations reformulated for the mean flow variables by introducing a Reynolds decomposition and using the Favre average for the total energy and the velocity field, whereas the time average is adopted for the pressure and the density. The equations in differential form are

$$\frac{\partial \bar{\rho}}{\partial t} + \frac{\partial(\bar{\rho}\tilde{u}_j)}{\partial x_j} = 0 \tag{1}$$

$$\frac{\partial(\bar{\rho}\tilde{u}_i)}{\partial t} + \frac{\partial}{\partial x_j}(\bar{\rho}\tilde{u}_i\tilde{u}_j + \bar{p}\delta_{ij} - \sigma_{ij}) = 0 \tag{2}$$

$$\frac{\partial(\bar{\rho}\tilde{E})}{\partial t} + \frac{\partial}{\partial x_j}[\bar{\rho}\tilde{u}_j\tilde{E} + \tilde{u}_i(\bar{p}\delta_{ij} - \sigma_{ij}) + q_j] = 0 \tag{3}$$

and

$$\tilde{E} = \tilde{e} + \frac{\tilde{u}_i\tilde{u}_i}{2} + \frac{\widetilde{u_i''u_i''}}{2} \tag{4}$$

The pressure is defined according to the equation of state

$$\bar{p} = (\gamma - 1)\bar{\rho}\left(\tilde{E} - \frac{\tilde{u}_i\tilde{u}_i}{2} - \frac{\widetilde{u_i''u_i''}}{2}\right) \tag{5}$$

where $\gamma = 1.4$.

The constitutive equations of the components of the total stress tensor and the total heat flux vector (that account for the laminar and turbulent contributions) are

$$\sigma_{ij} = (\bar{\mu} + \mu_t)\left(2\tilde{S}_{ij} - \tfrac{2}{3}\tilde{S}_{ll}\delta_{ij}\right) - \tfrac{2}{3}\bar{\rho}k\delta_{ij}$$

$$q_j = -\gamma\left(\frac{\bar{\mu}}{Pr} + \frac{\mu_t}{Pr_t}\right)\frac{\partial \tilde{e}}{\partial x_j}$$

where the molecular viscosity $\bar{\mu}$ is determined through the semiempirical Sutherland law, whereas the turbulent viscosity is defined as $\mu_t = C_\mu \bar{\rho}k^2/\epsilon$.

Turbulence Modeling

Turbulence is accounted for by means of a two-equation k–ϵ model that accounts for the near-wall effects. In general, two-equation turbulence models are expected to better predict the turbulent behavior of the flow with respect to zero- and one-equation models.[5] However, a critical issue when using k–ϵ models is the treatment of the solid boundaries where the turbulence is strongly affected by molecular effects.

The model we employ is based on the solution of the transport equations for the turbulence kinetic energy ($k = \widetilde{u_i''u_i''}/2$) and its

dissipation rate [$\epsilon = 2(\bar{\mu}/\bar{\rho})\,\overline{S'_{ij}S'_{ij}} - \frac{2}{3}(\bar{\mu}/\bar{\rho})\,\overline{S'_{ll}S'_{ll}}$], whose differential form is

$$\frac{\partial(\bar{\rho}k)}{\partial t} + \frac{\partial(\bar{\rho}k\tilde{u}_j)}{\partial x_j} = \frac{\partial}{\partial x_j}\left[\left(\bar{\mu} + \frac{\mu_t}{\sigma_k}\right)\frac{\partial k}{\partial x_j}\right] + P_k - \bar{\rho}\epsilon + \Pi_c \tag{6}$$

$$\frac{\partial(\bar{\rho}\epsilon)}{\partial t} + \frac{\partial(\bar{\rho}\epsilon\tilde{u}_j)}{\partial x_j} = \frac{\partial}{\partial x_j}\left[\left(\bar{\mu} + \frac{\mu_t}{\sigma_\epsilon}\right)\frac{\partial \epsilon}{\partial x_j}\right] + P_\epsilon - \Phi_\epsilon \tag{7}$$

where

$$P_k = \left(2\mu_t\bar{S}_{ij} - \tfrac{2}{3}\mu_t\bar{S}_{ll}\delta_{ij} - \tfrac{2}{3}\bar{\rho}k\delta_{ij}\right)\bar{S}_{ij}$$

$$P_\epsilon = C_{\epsilon_1}(\epsilon/k)P_k, \qquad \Phi_\epsilon = C_{\epsilon_2}\bar{\rho}(\epsilon^2/k)$$

Reference 7 shows that the compressibility effects on turbulence (Π_c) play a role in very high Mach number flows dominated by strong shock-wave/boundary-layer interactions. This is not the case for supersonic ($M_\infty \approx 2$) missile configurations, and we have completely neglected the compressibility effects in all computations.

In the near-wall regions, turbulence models usually employ wall functions,[10] thus allowing the use of rather coarse grids. However, this approach is not valid in the presence of 1) a strong streamline curvature, 2) an adverse pressure gradient, 3) flows where molecular transport is significant, 4) separated flows, and 5) the influence of crossflow, etc. In all of these circumstances, and in particular for the type of flow we are interested in, the models require a consistent asymptotic behavior at the wall, as shown in Refs. 9 and 11. Consequently, we have taken into account low Reynolds effects, which allow the integration of the turbulence model equations directly to the wall by means of algebraic damping functions to enforce the asymptotic consistency of the near-wall turbulence. This amounts to introducing a functional dependency of both C_μ and C_{ϵ_2} on (Re_t), thus yielding

$$C_\mu = 0.09\left(1 + 3.45/\sqrt{Re_t}\right)\tanh(y^+/80)$$

$$C_{\epsilon_2} = 1.83\left[1 - \tfrac{2}{9}\exp\left(-Re_t^2\right)\right][1 - \exp(-y^+/4.9)]^2$$

where y^+ is the viscous wall coordinate and $Re_t = \bar{\rho}k^2/\epsilon\bar{\mu}$.

Numerical Method

The approach followed is based on a finite volume multiblock formulation, which uses a spatial discretization of the inviscid fluxes based on the adaptive dissipation method[12] and a cell-centered evaluation of the viscous contribution. At the block interfaces, we have implemented a coupling algorithm that ensures the flux conservation and the continuity of the vector of unknowns.[13,14] In general, supersonic flows around slender bodies at incidence are characterized by local phenomena (such as leeside vortices, crossflow recirculation, etc.) that require the use of locally refined grids, mainly in the leeside region. We have then implemented a local grid refinement (LGR) technique to accurately resolve all of the detail of the crossflow without losing computational efficiency. In particular, LGR has been developed in such a way that each block can be refined independently of the others.[15]

To increase the computational efficiency, we have also implemented a physical operator adaptation strategy that allows the solution for different equations in the different blocks. In particular, we introduce viscous blocks, which extend from the body surface up to a distance of about one diameter in the radial direction, where the RANS equations are solved; the diffusion effects are assumed to be negligible in the outer region, and we have introduced Euler blocks where the Euler equations are solved.

The discretized equations are integrated in time by means of an explicit Runge–Kutta algorithm. However, when using two-equation turbulence models, the system of governing equations is stiff due to the disparity between the turbulence and fluid-dynamic timescales, and the time integration may require, in principle, an extremely small time step. To reduce such a problem, we have introduced a precondition matrix that has the effect of scaling all of the characteristic times to the same order[9] and depends on the Jacobian of the k–ϵ source terms. For computational efficiency, we have used a partial Jacobian by neglecting the dependency of the wall damping functions on $\bar{\rho}k$ and $\bar{\rho}\epsilon$ (Ref. 9).

In general, the turbulence model equations are loosely coupled with the set of governing equations: The coupling occurs mainly through the turbulent viscosity. For numerical purposes one can then assume that these equations are decoupled. Indeed, Kunz and Lakshminarayana[16] have shown that (numerically) coupling the turbulence model equations and the mean flow equations affects neither the accuracy nor the convergence of the solution. Therefore, we have devised a numerical strategy that uses a five-stage semi-implicit Runge–Kutta algorithm and that solves the complete set of equations in a split fashion, i.e., we first solve the mean flow equations and then the k–ϵ equations.

Results

The objective of the simulations is to discuss the main physical and numerical issues to understand the effects of crossflow and turbulence on the vortex flow around a supersonic missile configuration.

The simulated test cases correspond to the supersonic flow at fixed Mach and Reynolds numbers ($M_\infty = 2$ and $Re_D = 1.6 \times 10^5$) and different angles of attack ($\alpha = 0$, 5, and 20 deg). The geometry of the body is an ogive cylinder (of total length $L = 270$ mm and diameter $D = 30$ mm) with a circular ogive of 90 mm. The test cases have been selected for the availability of detailed experimental data (in terms of flow visualization and surface and crossflow pressure distributions), which allow the assessment of the validity of the numerical model. Pagan et al.[3] performed experiments for two different flow conditions: natural transition and forced transition triggered by means of a strip located at $x/D = 1$. At the investigated angles of attack, the experiments indicated that transition did occur at the strip location (under forced transition), whereas the flow was found to remain laminar for natural transition at low incidence (at least for $\alpha \leq 10$ deg).

We have performed several computations assuming either laminar conditions (corresponding to the natural transition of the experiments, at least for the low incidence cases) or turbulent conditions with prescribed transition either at the (experimental) strip location or along a transition line (Fig. 1).

Grid Sensitivity Analysis

Before discussing the effects of the crossflow and turbulence, we address the problem of selecting a computational mesh when both accuracy and efficiency constraints have to be met. The applications discussed refer to the flow around simple axisymmetric slender bodies at incidence. The controlling phenomena are mainly related to the formation of leeside vortices (generated primarily through an inviscid mechanism) and their interaction with

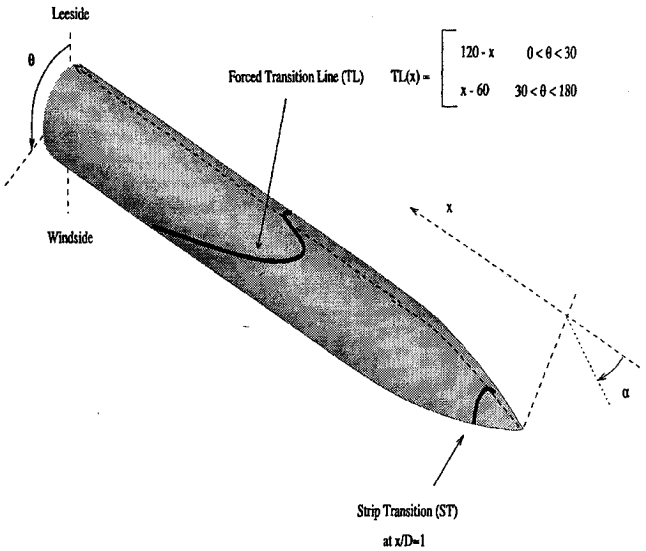

Fig. 1 Ogive-cylinder configuration and definitions of forced transition locations.

Table 1 Grid dimensions and aerodynamics coefficients

Grid	Viscous blocks			Inviscid blocks			Lift	Drag	Pitch
	N_x	N_r	N_θ	N_x	N_r	N_θ			
G_1	64	32	12	64	32	12	2.5102	1.1433	−3.5442
G_2	128	64	24	64	32	24	2.4926	1.0860	−2.9852
G_3	128	64	40	64	32	20	2.4760	1.0793	−2.9582
G_4	128	96	80	64	32	20	2.4719	1.0771	−2.9266
G_5	256	64	40	64	32	20	2.4745	1.0809	−2.9432

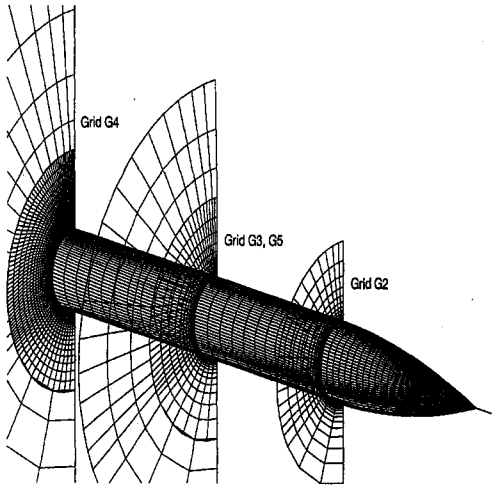

Fig. 2 Cross sections of computational grids used for the grid sensitivity analysis.

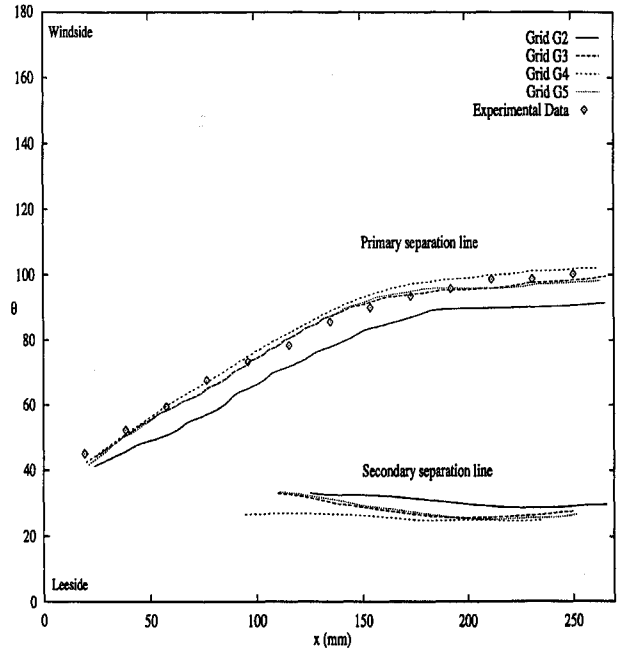

Fig. 3 Primary and secondary separation lines; α = 20 deg, laminar computations.

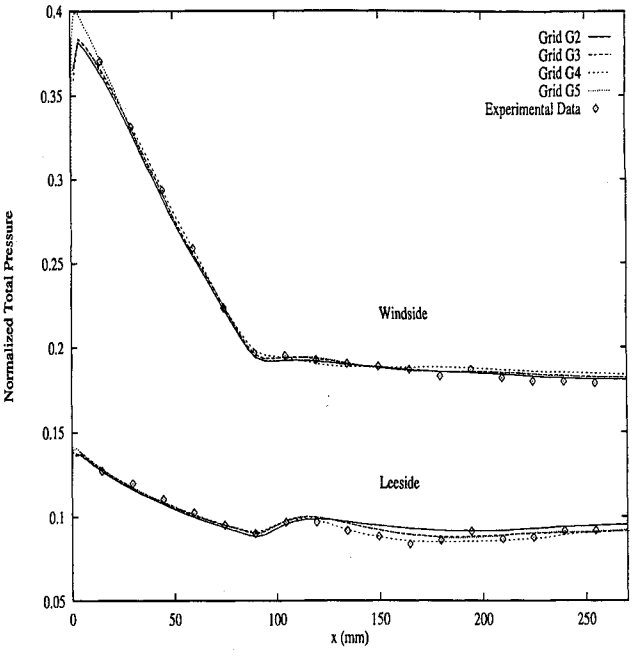

Fig. 4 Surface pressure distribution on the symmetry plane; α = 20 deg, laminar computations.

the vorticity production mechanism in the boundary layer. Then, for accuracy, an adequate computational mesh should permit the resolution of the details of the flow in a region that extends (in the radial direction) from the body up to a distance approximately equal to the body cross section and should be sufficiently refined in the circumferential direction at the leeside. Vice versa, for efficiency, an adequate grid should be such that a solution is obtained in a reasonable computational time (1–2 h of supercomputer CPU time). We reason that to satisfy these constraints a grid should not have more than 0.5×10^6 cells. To establish the influence of the mesh we have performed a grid study by considering five grids, whose section in the crossflow plane is shown in Fig. 2. Grid G_1 has $64 \times 32 \times 12$ cells with an equally spaced distribution in θ and radial stretching; grid G_2 has $128 \times 64 \times 24$ cells, and it was obtained from G_1 by simply doubling the number of cells in all directions, thus retaining the same cell-aspect-ratio distributions. Grid G_3 is obtained from G_2 by a zonal refinement in the vortex dominated region, which is the region that extends for $0 \text{ deg} \leq \theta \leq 120$ deg (as found in the simulations); N_θ is (roughly) doubled in the viscous blocks, whereas it has been reduced by a factor of two (with respect to G_2) in the inviscid blocks. Grid G_4 is obtained from G_3 by halving the mesh spacing in both the radial and circumferential directions. Grid G_5 was obtained from grid G_3 by doubling the number of cells in the streamwise direction (N_x). The main parameters of the grids are given in Table 1.

The analysis of grid sensitivity has been carried out for all test cases (0, 5, and 20 deg); however, due to space limitations we discuss only the 20-deg case. To isolate the influence of the grid from the effects of turbulence, we have not forced any transition and we have assumed laminar conditions. We recall that at high incidence the experiments indicate that the flow may not remain laminar; nonetheless, the experiments do show very little influence of turbulence on the flowfield at high incidence, and the computed results will be compared with the natural transition measurements.

The 20-deg test case exhibits a very complex flow structure with multiple crossflow separations and reattachments and the formation of primary and secondary vortices. The computed primary and secondary separation lines are shown in Fig. 3; we observe that grids G_3, G_4, and G_5 show differences on the order of 1–2%. The same is true for the streamwise surface pressure distributions at the leeside and windward planes that are shown in Fig. 4. Likewise, the circumferential distribution (Fig. 5) shows that the level of the pressure plateau and the recompression at leeside are well predicted on G_3, G_4, and G_5; in addition, the results show the occurrence of a crossflow shock

Table 2 Critical points in the crossflow topology at 20 deg of incidence

	Grid	N	S	S'
Present results	G_2	8	3	12
	G_3, G_5	10	3	16
	G_4	12	5	16
Ref. 5		18	11	16
Ref. 3		8	3	12

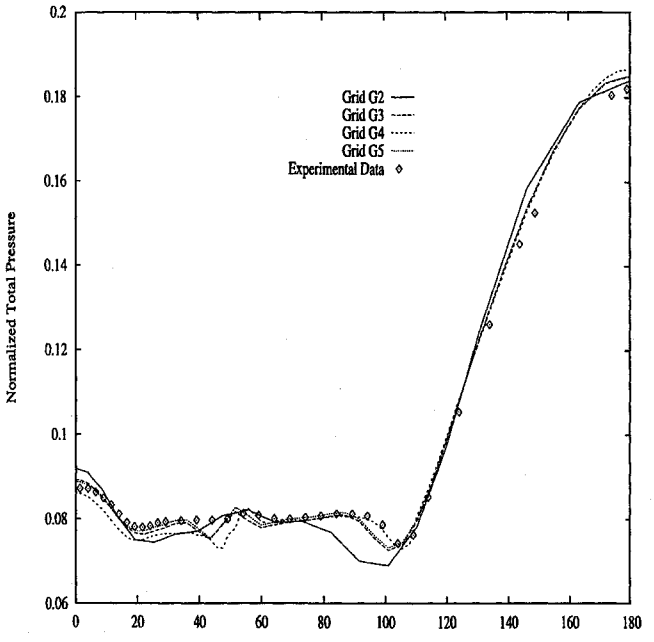

Fig. 5 Surface pressure distribution in a crossflow; $\alpha = 20$ deg, laminar computations; $x/D = 7$.

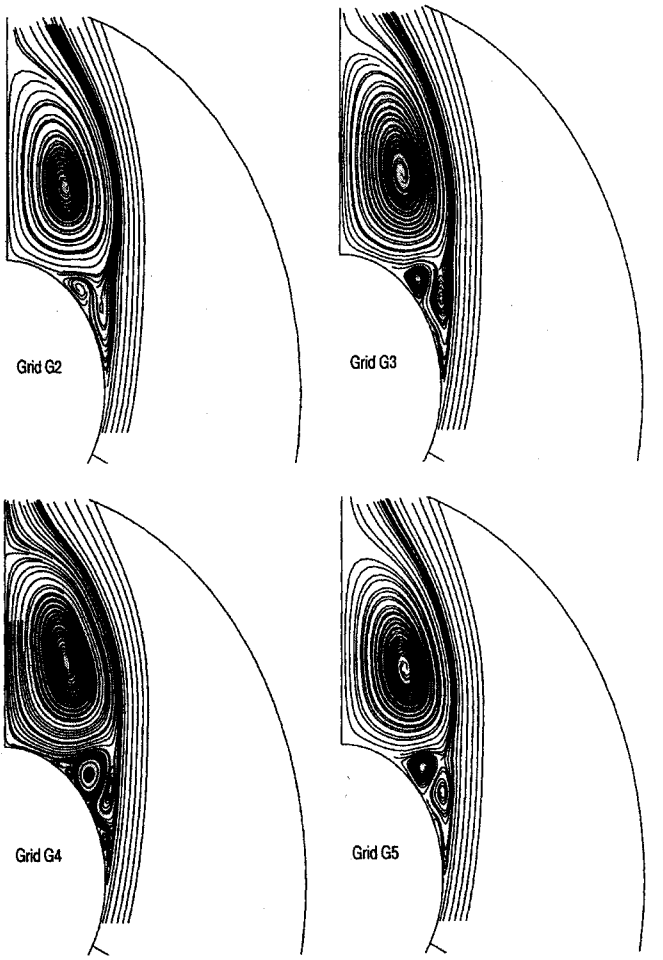

Fig. 6 Crossflow streamlines at $x/D = 7$; $\alpha = 20$ deg, laminar computations.

not observed in the experiments. An indication of grid convergence of the results can also be inferred from the aerodynamic coefficients (lift, drag, and pitching moment), which are reported in Table 1. The results show that the variation (with respect to the solution on the base grid G_3) in the coefficients, indeed, is not significant.

The vortical flow structure is usually analyzed in terms of the streamline pattern in the crossflow plane. In such a plane the flow typically exhibits crossflow separation and reattachment, and the critical point theory can be used to interpret the flow pattern. The type of critical points, i.e., nodes, half-nodes, saddles, half-saddles, etc., and their character (stable or unstable) depend on the stretching and compression of the vortex core. From a mathematical point of view, the classification of the critical points requires that the relation between the divergence and Jacobian of the (cross)flow in the crossflow plane must be determined.[5,17] In addition, the following relation (hereafter referred to as the topological relation) is also found to hold:

$$\Sigma N + \Sigma N'/2 - \Sigma S - \Sigma S'/2 + 1 = 0$$

The computed results verify the topological relation independently of the selected grid (Table 2). However, the total number of nodes, saddles, etc., is not grid independent, with the obvious consequence that one may arrive at a different interpretation of the crossflow topology when analyzing a computed solution that is not grid independent. The computed crossflow topology depends on both the radial and circumferential resolutions as the results in Table 2 indicate; as Fig. 6 shows, near grid independence is achieved for $\Delta r \approx \mathcal{O}(10^{-2}D)$ and $\Delta\theta \approx 1$–3 deg. The differences between the predicted topology and the experimental one in all likelihood can be ascribed to some uncertainties in the measurements that make use of a five-hole pressure probe whose accuracy can be estimated in the range of 5–10% in the core of the intense vortices. The discrepancy with the topology predicted by Moschetta et al.[5] might be due to the parabolizing assumption, which may produce some differences with full Navier–Stokes predictions in the leeside region even for simple configurations.[6]

Crossflow Analysis

We now discuss the effects of incidence and turbulence on the crossflow structure. In particular, we have considered three values of the incidence: 0 (not reported due to space limitations), 5, and 20 deg, and both laminar and turbulent conditions, as in the experiments of Ref. 3. All computations were performed on grid G_3.

To characterize the influence of the crossflow on the surface flow pattern, we show (Fig. 7) the predicted skin-friction lines together with the computed and experimental oil flow visualization (where the computed one has been obtained by a linear integral convolution of the wall shear stress[18]). At 5 deg, the flow exhibits primary and secondary separations that roll up to form two counter-rotating vortices (on each side of the symmetry plane). The positions of the predicted and experimental primary separation lines are in good agreement (Fig. 7a). At 20 deg, the complexity of the vortical flow structures increases with the occurrence of multiple separations and reattachments. The primary separation line is displaced toward the windward side (at $x/D = 7$ the displacement is about 10 deg), whereas the secondary one moves toward the leeside (at $x/D = 7$ the displacement is about 30 deg). The rollup of the separation surfaces gives rise to three vortices of finite sizes and two tiny structures in the proximity of the wall. The qualitative comparison between the computed and experimental oil flow visualizations (Fig. 7b) is impressive.

To characterize the influence of turbulence on the surface flow pattern, we show the computed skin-friction lines for the forced transition condition at $x/D = 1$. As Fig. 7c shows, at 5-deg turbulence is found to inhibit separation, whereas at 20 deg (Fig. 7d), the structure of the flow is rather insensitive to turbulence. The surface pressure distribution at $x/D = 7$ is shown in Fig. 8, where we show

a) Computed oil flow visualization

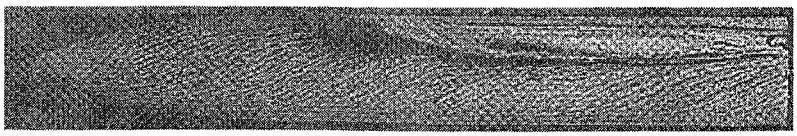

b) Experimental oil flow visualization

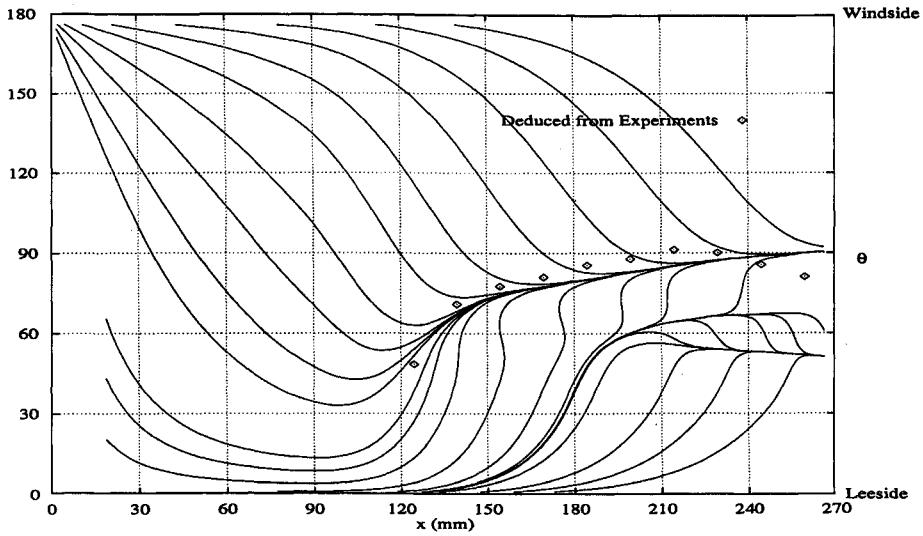

c) Skin-friction patterns

Fig. 7a Incidence at 5 deg, laminar computations, α = 5 deg.

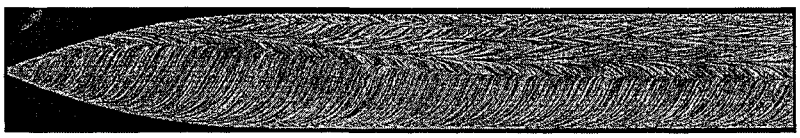

a) Computed oil flow visualization

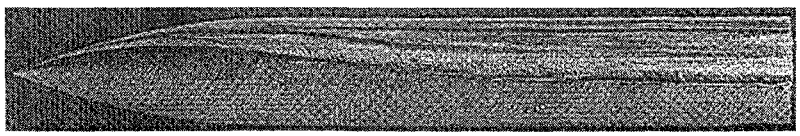

b) Experimental oil flow visualization

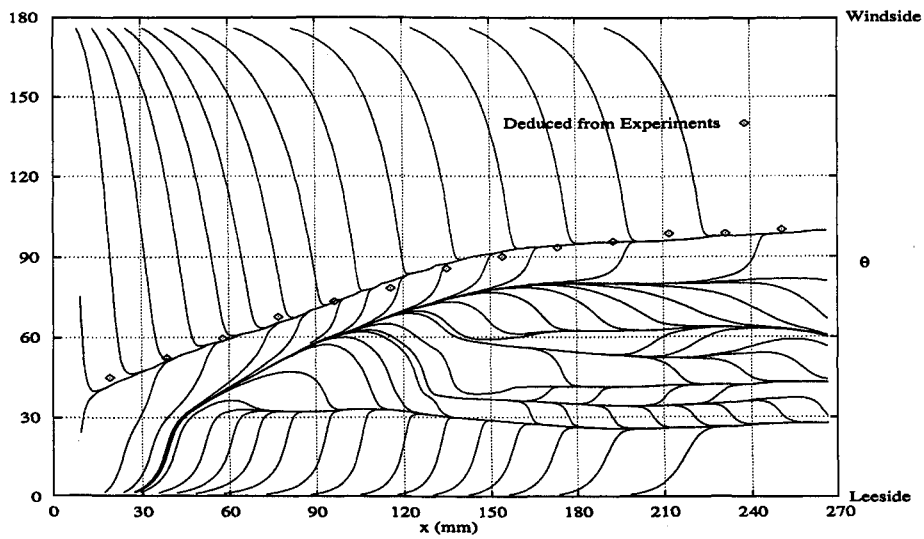

c) Skin-friction patterns

Fig. 7b Incidence at 20 deg, laminar computations, α = 20 deg.

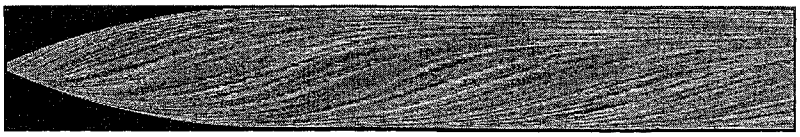

a) Computed oil flow visualization

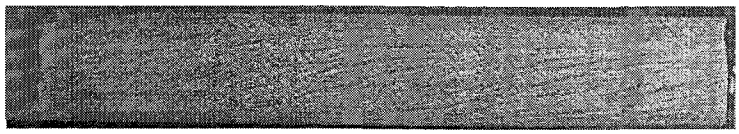

b) Experimental oil flow visualization

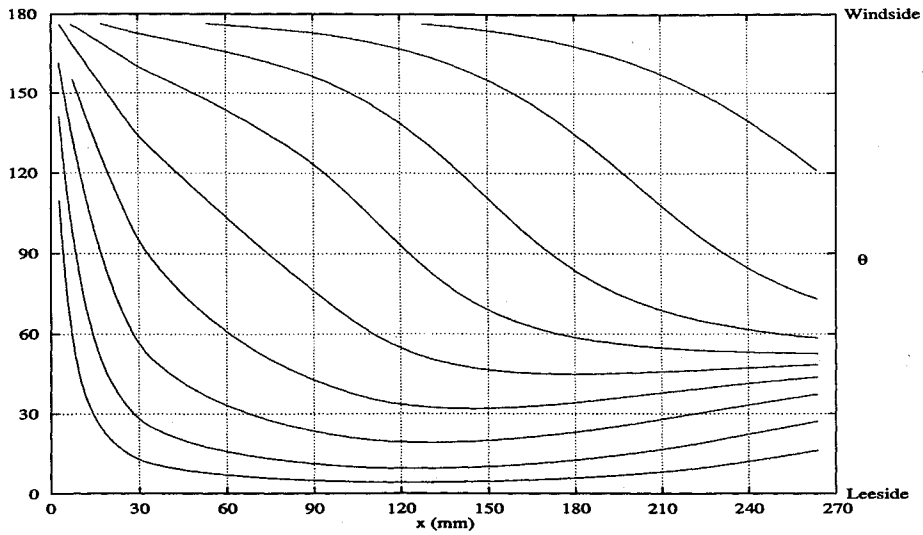

c) Skin-friction patterns

Fig. 7c Incidence at 5 deg, turbulent computations (strip transition), $\alpha = 5$ deg.

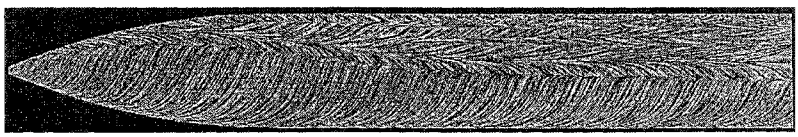

a) Computed oil flow visualization

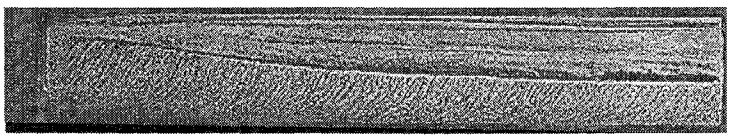

b) Experimental oil flow visualization

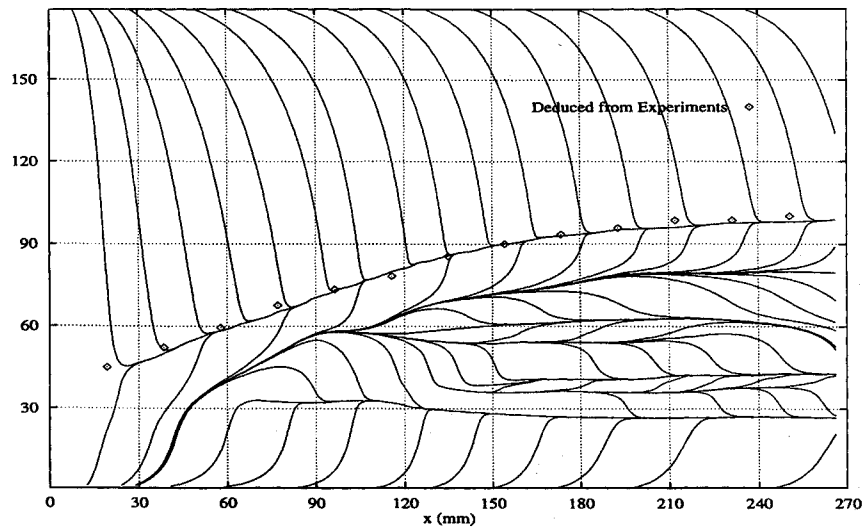

c) Skin-friction patterns

Fig. 7d Incidence at 20 deg, turbulent computations (strip transition), $\alpha = 20$ deg.

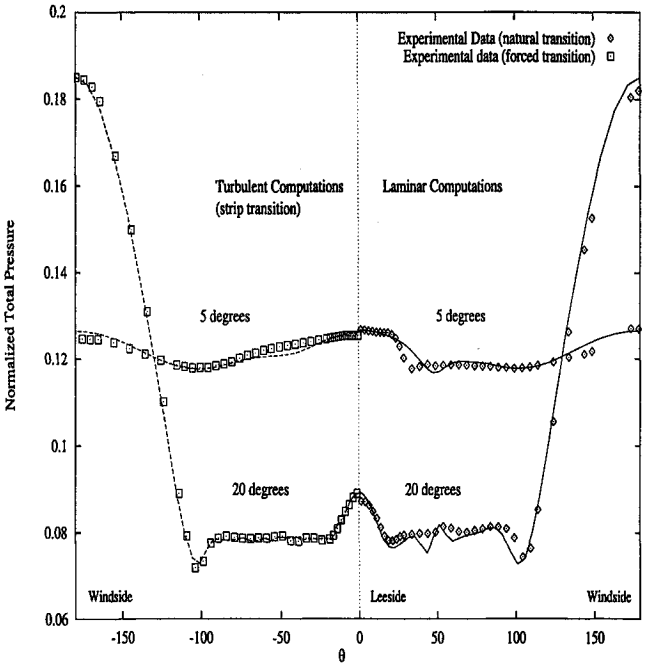

Fig. 8 Surface pressure distribution at $x/D = 7$.

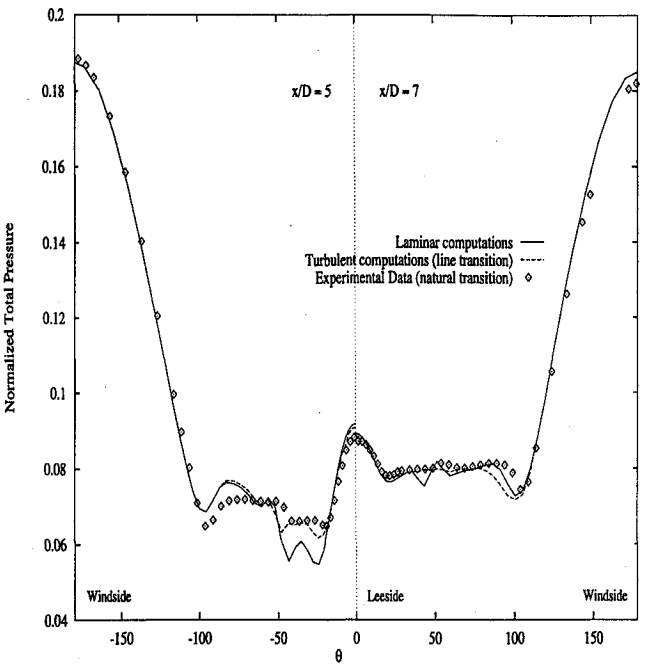

Fig. 10 Surface pressure distribution, $\alpha = 20$ deg.

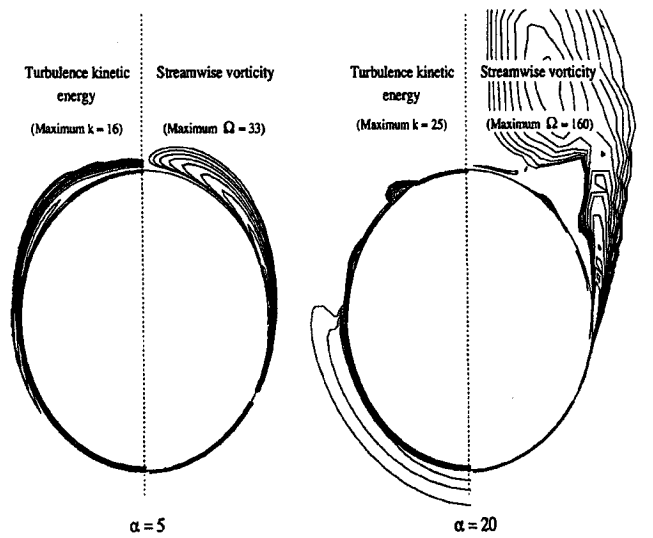

Fig. 9 Turbulence kinetic energy and vorticity contour lines at $x/D = 7$ (strip transition).

both the laminar (corresponding to the natural transition condition of the experiment) and turbulent (the strip transition condition) results for $\alpha = 5$ and 20 deg. For the laminar conditions, we observe that as the incidence increases the strength of the leeside vortices increases and a plateau pressure arises, whose value is lower at higher incidence. In addition, the increase in the primary vortex intensity produces a strong recompression at leeside, whereas the expansion at windside is rather insensitive to the incidence. The computed results show, overall, good agreement with the experiments both in the pressure level and in the rate of recompression and expansion. Some discrepancies are noticeable at 5 deg in the prediction of the pressure minimum; at 20 deg the computations show a recompression followed by an expansion immediately past the secondary separation not observed in the experiments. The forced (strip) transition results confirm that turbulence affects the surface pressure distribution only at low incidence; at 20 deg, the laminar and turbulent distributions are nearly the same.

In Fig. 9, we show the turbulence kinetic energy and streamwise vorticity at $x/D = 7$ for $\alpha = 5$ and 20 deg. At low incidence k is higher and Ω is lower, whereas at high incidence the opposite is true. At 5 deg, the leeside vortex is not intense, and we reason that the dissipation of turbulence kinetic energy is low. At 20 deg, strong crossflow acceleration and vortex stretching (with the formation of secondary vortices) generate streamwise vorticity; hence the dissipation of turbulence kinetic energy that inhibits the production of k.

To complete our analysis we have carried out an additional turbulent simulation triggering transition along a line in an attempt to understand the discrepancies (already discussed) between the natural transition measurements and the laminar computations at 20 deg. Cebeci and Chen[19] have shown the influence of the crossflow on the laminar–turbulent transition for a prolate spheroid at incidence. In particular, they have shown that transition is delayed in the windward region where the flow is accelerating while it moves upstream in the leeward region due to flow deceleration. We also recall that the primary separation line, the leeside recompression, and the level of the plateau pressure are rather well predicted by a laminar assumption. We have then assumed that transition occurs after the primary separation and, therefore, we have forced transition along a line as shown in Fig. 1. The computed surface pressure distributions at $x/D = 5$ and 7 (Fig. 10) indicate an improvement in the predictions and in particular the weakening of the crossflow shock (found in the laminar computations).

Conclusions

The influence of crossflow and turbulence on the vortical supersonic flow around a slender body of revolution has been studied. In particular, we have analyzed 1) the dependency of the numerical predictions on the grid resolution, 2) the effects of the crossflow on skin-friction patterns and surface pressure distributions, and 3) the influence of turbulence, vortex strengths, and transition location.

The grid sensitivity analysis shows that, as far as separation and reattachment are concerned, the flowfield is affected mainly by the resolution in the circumferential direction; on the other hand, the crossflow structure depends on both the radial and circumferential resolutions. The critical point analysis has been used for the interpretation of the crossflow topology, and we have shown that the topological relation (that exists for the critical points) cannot be used for assessing grid convergence.

The establishment of the flowfield depends on the relative importance of the boundary-layer development along the body, affecting the turbulence kinetic energy production (TKP) and the streamwise vorticity production (VP) that is related to the crossflow acceleration. At low incidence TKP > VP, and the flow is dominated by turbulence; at high incidence TKP $\leq$ VP, and the flow is affected by the strength of the vortical structures rather than turbulence. At

very low incidence, the latter inhibits separation, whereas at high incidence, the effect of turbulence is that of displacing the primary separation toward the leeside.

An attempt to account for natural transition due to crossflow instability has also been made by triggering transition along a line. The computed results seem to indicate that at high incidence a laminar flow assumption may be questionable past the primary separation. However, the aspect of transition needs to be further investigated.

Acknowledgments

We acknowledge J. Delery for helpful discussions and for providing the experimental data; we also acknowledge the help of B. Sikorsky in the generation of the computed oil flow visualizations.

References

[1]Moore, F. G., "Engineering Codes for Aeropredictions: State-of-the-Art and New Methods," Special Course on Missile Aerodynamics, AGARD R-804, June 1994, pp. 2.1–2.82.

[2]Hartmann, K., "Experimental Data Base for Computer Program Assessment," Fluid Dynamic Panel, FDP WG-04, AGARD AR-138, 1979, pp. C1.1–C1.37.

[3]Pagan, D., Molton, P., and Delery, J., "Basic Experiment on a Superscript Vortex Flow Around a Missile Body," *Journal of Spacecraft and Rockets*, Vol. 29, No. 3, 1992, pp. 373–378.

[4]Degani, D., and Schiff, L. B., "Computation of Turbulent Supersonic Flows Around Pointed Bodies Having Crossflow Separation," *Journal of Computational Physics*, Vol. 66, 1986, pp. 173–196.

[5]Moschetta, J. M., Lafon, A., and Deniau, H., "Numerical Investigation of Supersonic Vortical Flow About a Missile Body," *Journal of Spacecraft and Rockets*, Vol. 32, No. 5, 1995, pp. 765–770.

[6]Deniau, H., Lafon, A., and Moschetta, J. M., "Progress in the Development of Turbulence Models for the Computation of 3D Supersonic Flow with Crossflow Separation," AIAA Paper 95-0090, Jan. 1995.

[7]Birch, T. J., Qin, N., and Jin, X., "Computation of Supersonic Viscous Flows Around a Slender Body at Incidence," AIAA Paper 94-1938, June 1994.

[8]Weinacht, P., and Sahu, J., "Navier Stokes Predictions of Missile Aerodynamics," Special Course on Missile Aerodynamics, AGARD R-804, June 1994, pp. 6.1–6.48.

[9]Grasso, F., and Falconi, D., "On High Speed Turbulence Modeling of Shock Wave-Boundary Layer Interaction," *AIAA Journal*, Vol. 31, No. 7, 1993, pp. 1199–1206.

[10]Viegas, J. R., Rubesin, M. W., and Horstman, C. C., "On the Use of Wall Functions as Boundary Conditions for Two-Dimensional Separated Compressible Flows," AIAA Paper 85-0180, Sept. 1985.

[11]Speziale, G. C., and Sarkar, S., "A Preliminary Compressible Second-Order Closure Model for High Speed Flows," NACA Rept. 181875, Feb. 1989.

[12]Jameson, A., "Transonic Flow Calculations," Dept. of Mechanical and Aerospace Engineering, MAE Rept. 1651, Princeton Univ., Princeton, NJ, 1983.

[13]Quarteroni, A., "Domain Decomposition Methods for Systems of Conservation Laws: Spectral Collocation Approximation," Inst. for Computer Applications in Science and Engineering, ICASE Rept. 89–5, May 1989.

[14]Fatica, M., and Grasso, F., "Numerical Solutions of Compressible Viscous Flows Using Multidomain Techniques," *Lecture Notes on Numerical Fluid Mechanics*, Vol. 35, Vieweg Verlag, Braunschweig, Germany, 1992, pp. 170–179.

[15]Amato, M., Iaccarino, G., and Paparone, L., "Automatic Local Grid Refinement for Multiblock Solvers," *Proceedings of the 5th International Conference on Numerical Grid Generation 96*, Starkville, MS, 1996.

[16]Kunz, R. F., and Lakshminarayana, B., "Stability of Explicit Navier–Stokes Procedures Using k–ϵ and k–ϵ/Algebraic Reynolds Stress Turbulence Models," *Journal of Computational Physics*, Vol. 103, 1992, pp. 141–195.

[17]Visbal, M. R., and Gornier, R. E., "Crossflow Topology of Vortical Flows," *AIAA Journal*, Vol. 32, No. 5, 1994, pp. 1085–1087.

[18]Cabral, B., and Leedom, L.,"Imaging Vector Fields Using Line Integral Convolution," *SIGGRAPH Proceedings*, Association for Computing Machinery, ACM SIGGRAPH, 1993, pp. 263–272.

[19]Cebeci, T., and Chen, H. H., "Prediction of Transition on Airfoils with Separation Bubbles, Swept Wings and Body of Revolution at Incidence," *Aerodynamic Flows*, Vol. 4, Springer–Verlag, New York, 1990.

R. M. Cummings
Associate Editor